Volume 14
Number 8
21 April 2026
Pages 1867-2144

Biomaterials Science

rsc.li/biomaterials-science

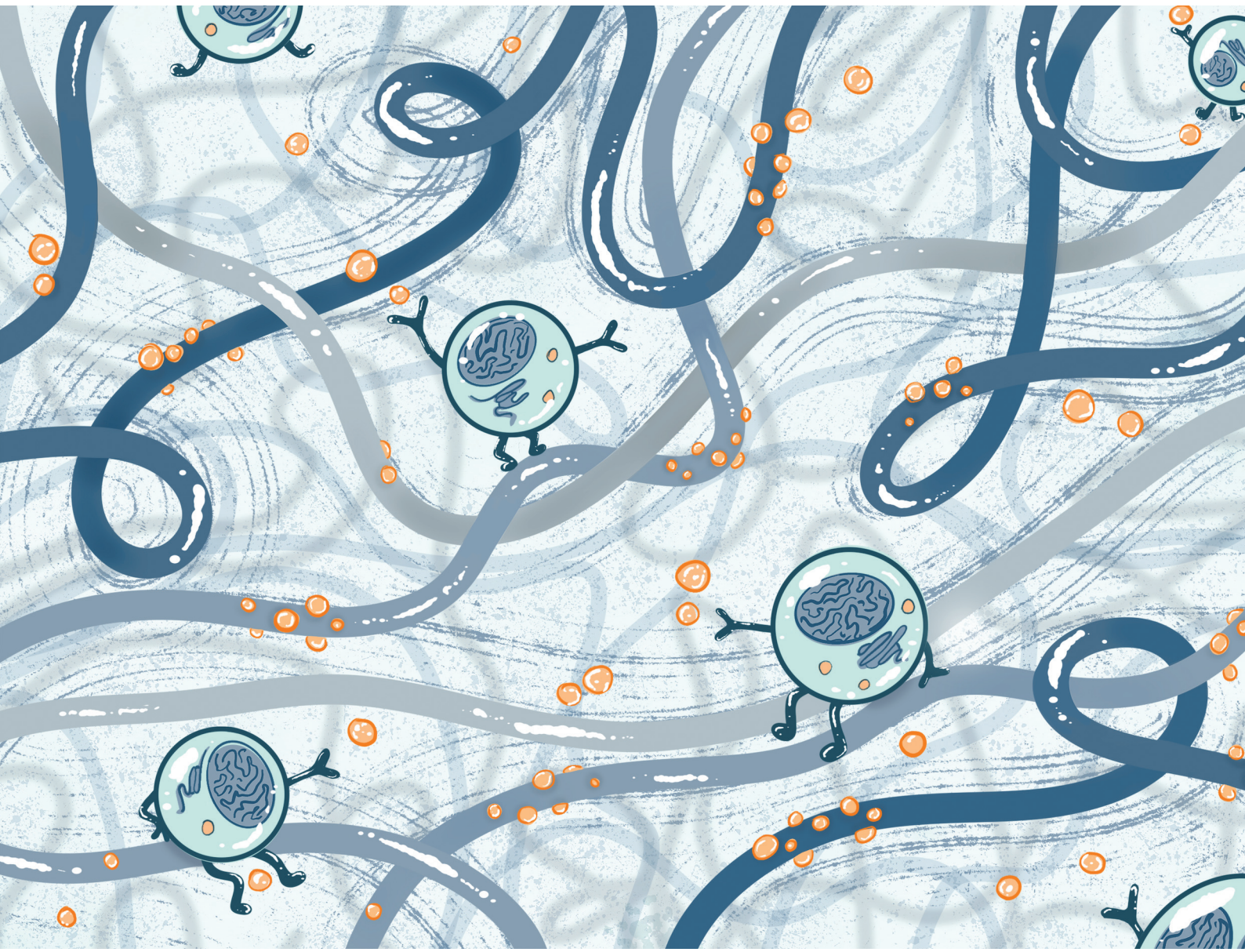

ISSN 2047-4849

ROYAL SOCIETY OF CHEMISTRY

PAPER

Treena Livingston Arinzeh, Santiago Correa *et al.*
Modular noncovalent functionalization of electrospun piezoelectric scaffolds with bioactive nanocarriers

European Society for Biomaterials

Biomaterials Science

ROYAL SOCIETY OF CHEMISTRY

PAPER

View Article Online
View Journal | View Issue

Cite this: *Biomater. Sci.*, 2026, **14**, 1963

Modular noncovalent functionalization of electrospun piezoelectric scaffolds with bioactive nanocarriers

Sarah Payne Bortel, [a] Sumayia Saif Jaima Chowdhury, [a] Jeremy Cheng,[a] Daniella Uvaldo,[a] Mackenzie Wright,[b] Anna Marie Kylat,[a] Treena Livingston Arinzeh*[a] and Santiago Correa *†[a,c]

Electrospun scaffolds offer a promising platform for immune-instructive materials, but stable and modular functionalization with bioactive signals remains a technical challenge. Here, we develop a surface coating strategy for electrospun scaffolds that consist of poly(vinylidene fluoride-trifluoroethylene) (PVDF-TrFE), a piezoelectric polymer, using electrostatic adsorption of charged nanoparticles. We show that under certain conditions, these piezoelectric scaffolds are suitable substrates for electrostatic self-assembly, and that the density of nanoparticle coatings can be tuned by adjusting buffer pH, ionic strength, and nanoparticle concentration. This approach enables robust and uniform coating with both polymeric nanoparticles and soft nanocarriers such as liposomes, without requiring covalent surface modification of the scaffold. Liposome-coated scaffolds are cytocompatible with adherent epithelial and suspension immune cells and support lipid exchange at the cell–material interface. Using a supramolecular tethering strategy, we use liposome coatings to present interleukin-15 (IL-15) from the scaffold surface and demonstrate localized, sustained cytokine signaling. Together, these findings establish a modular approach for post-fabrication, noncovalent scaffold functionalization with bioactive nanocarriers, offering new opportunities for tissue and immune engineering.

Received 24th October 2025,
Accepted 26th February 2026

DOI: 10.1039/d5bm01563d

rsc.li/biomaterials-science

Introduction

Instructive biomaterials that modulate immune cell function are needed across regenerative medicine, cancer immunotherapy, and *ex vivo* cell engineering. Local delivery from a material interface can reduce systemic immune-related adverse effects,[1–6] yet presenting potent immune signals such as cytokines in a sustained, spatially confined manner remains difficult. Cytokines are rapidly degraded *in vivo*,[7–9] and often act most effectively when recognized in a membrane-proximal configuration,[9,10] which complicates controlled use in biomaterial systems. As a result, there is a need for tunable biomaterials to locally present cytokines at the cell interface.

Prior strategies to localize bioactive cues within biomaterials include bulk encapsulation,[11] covalent tethering,[12] and immobilization onto nanoparticles (NPs),[13] each with tradeoffs in spatial precision, loading efficiency, and functional potency. In soluble form, cytokines typically require repeated dosing or chemical modification to extend half-life, with associated losses in activity.[14,15] Liposomes offer a promising alternative because they can carry fragile proteins,[16,17] limit systemic exposure,[18] and mimic aspects of membrane-bound ligand display.[19,20] However, methods to integrate liposomes uniformly and stably onto scaffolds, while preserving cell access to surface-presented cargo, remain limited.[21–25]

Electrospun scaffolds are widely used in immunoengineering and tissue regeneration due to their high surface area,[26] tunable architecture,[27–29] and mechanical responsiveness.[30–33] These features make electrospun scaffolds attractive for presenting bioactive signals at the cell interface, yet reliably achieving such presentation remains challenging. Addressing this gap requires a noncovalent surface functionalization approach that preserves scaffold architecture and maintains nanocarrier bioactivity and cell accessibility. We hypothesized that electrostatic self-assembly principles established in layer-by-layer systems could be adapted to electrospun fibers to tether charged nanoparticles without covalent chemistry.[34,35] Piezoelectric polymers like poly(vinylidene fluoride-trifluoroethylene) (PVDF-TrFE) present a unique opportunity in this context: mechanical deformation can induce surface charge on the fibers, creating favorable conditions for adsorption of oppositely charged species.[36–39]

[a]*Department of Biomedical Engineering, Columbia University, New York, NY 10027, USA. E-mail: tla2132@columbia.edu, sc5159@columbia.edu*
[b]*Department of Biological Sciences, Columbia University, New York, NY 10027, USA*
[c]*Herbert Irving Comprehensive Cancer Center, Columbia University, New York, NY 10032, USA*
† Lead contact.

Here, we present a surface-functionalized scaffold system based on electrospun PVDF-TrFE fibers, designed for tunable electrostatic adsorption of charged polymeric and liposomal nanoparticles. We show that mechanically generated surface charge during loading, together with optimized buffer conditions to control pH and ionic strength, enables robust adsorption of both polymeric nanoparticles and soft lipid nanocarriers without covalent modification. The coated scaffolds remain cytocompatible and support three-dimensional cell culture of human endothelial kidney 293 (HEK293) and Jurkat T cells. Building on a supramolecular tethering strategy previously applied in hydrogel systems,[40] we noncovalently display interleukin-15 on scaffold-bound liposomes and demonstrate receptor signaling in a reporter cell line. This work establishes a modular, novel framework for post-fabrication functionalization of electrospun scaffolds to generate biomaterials enabling controllable, noncovalent presentation of bioactive nanocarriers for cell-instructive biomaterials.

Results and discussion

Tuning electrostatic adsorption of polymeric nanoparticles onto piezoelectric scaffolds

Electrostatic self-assembly offers a versatile strategy for surface functionalization, as exemplified by layer-by-layer (LbL) techniques that use alternating charged species to build well-defined interfaces.[41] While these approaches have been widely applied to planar or chemically modified substrates,[42–44] their applications to three-dimensional, electrospun fibrous scaffolds are less explored. We hypothesized that the surface charge of PVDF-TrFE[45] could support electrostatic charged nanoparticle adsorption without requiring covalent modification. PVDF-TrFE is a piezoelectric polymer that, when spun into fibrous scaffolds and annealed, can generate voltage outputs on the order of 100 mV to 1 V depending upon mechanical loading conditions.[30] To test this hypothesis, we investigated how nanoparticle composition and coating conditions influence their electrostatic adsorption onto these piezoelectric substrates.

To explore how nanoparticle surface properties influence scaffold adsorption, we compared two nanoparticle types: commercial carboxylate modified latex (CML) particles, which are stiff and smooth, and LbL-coated CML nanoparticles, which are expected to be softer and have a rougher surface due to their loopy, entangled polymer layers.[46] We generated cationic LbL nanoparticles by sequentially coating anionic CML particles with three polyelectrolyte layers: cationic poly(allylamine hydrochloride) (PAH), anionic poly(acrylic acid) (PAA), and a final layer of PAH. This multilayered coating increased the particle diameter from 117.4 ± 0.1 nm to 143.6 ± 0.5 nm, as measured by dynamic light scattering (SI Fig. 1A and B). Both particle types displayed narrow size distributions (PDI = 0.03 ± 0.01 or 0.05 ± 0.01, respectively) (SI Fig. 1D), and their high-magnitude zeta potentials (−52.00 ± 0.91 mV or +48.59 ± 2.02 mV, respectively) confirmed strong surface charge, making them appropriate for electrostatic adsorption (Fig. 1A).

To generate a suitable substrate for electrostatic adsorption, we fabricated electrospun PVDF-TrFE piezoelectric scaffolds. To facilitate electrostatic adsorption of nanoparticles, the substrate must carry a surface charge of opposite polarity to the adsorbing species.[35] Electrospun piezoelectric polymers like PVDF-TrFE offer a unique advantage in this context: they can generate surface charge in response to mechanical deformation due to changes in the polarization of aligned molecular dipoles.[47] The polarization domains of PVDF-TrFE scaffolds can be further enhanced through corona poling, a process in which exposure to a high-voltage electric field induces dipole alignment within the fibers. Mechanical deformation of the material induces local movement in the dipoles.[48–50] To ensure that poling did not alter scaffold morphology, we characterized fiber diameter by scanning electron microscopy (SEM). Corona poled (poled) and unpoled scaffolds exhibited comparable fiber diameters (1.69 ± 0.30 μm on poled scaffolds and 1.80 ± 0.51 μm on unpoled scaffolds, $p = 0.1942$) (SI Fig. 2).

To optimize scaffold coating, we compared two nanoparticle loading strategies on poled scaffolds: passive incubation and vacuum-assisted deposition. For passive incubation, scaffolds were submerged in nanoparticle solution without agitation. In contrast, the vacuum-assisted method was designed to introduce mechanical deformation during coating by sealing scaffolds in a tube filled with nanoparticle solution and applying negative pressure *via* syringe during repeated agitation to induce scaffold flexion. SEM revealed that passive incubation-based loading resulted in minimal nanoparticle adsorption onto the scaffold (Fig. 1B), whereas vacuum-assisted loading induced nanoparticle adsorption and more uniform coatings (Fig. 1C).

Although we observed that mechanical deformation of the scaffold enhanced nanoparticle adsorption, the overall coating density remained sparse across tested conditions. We hypothesized that, beyond surface charge effects, adsorption density may also depend on solution conditions known to modulate electrostatic interactions in layer-by-layer electrostatic assembly.[34,51,52] To test this, we investigated how solution pH and ionic strength influence nanoparticle adsorption, with the goal of optimizing coating conditions to achieve a thicker and denser coating.

We evaluated nanoparticle adsorption in three solution conditions designed to systematically vary pH and ionic strength: (1) deionized water (low ionic strength, unbuffered), (2) HEPES buffer (pH buffered, low ionic strength), and (3) HEPES buffer supplemented with NaCl (pH buffered, high ionic strength). 500 mM HEPES was selected as a zwitterionic buffer that maintains a pH of 7.5 while negligibly contributing to ionic strength, allowing us to stabilize the ionization states of the charged carboxyl and amine groups on the nanoparticle surfaces without altering the Debye screening length (λ_D).[35,53] To tune ionic strength independently, we added 400 mM NaCl to 500 mM HEPES, to evaluate an ionic strength of 0.4 M (λ_D = 0.48 nm) at pH 7.5. These conditions allowed us to independently assess how charge ionization and electrostatic screening

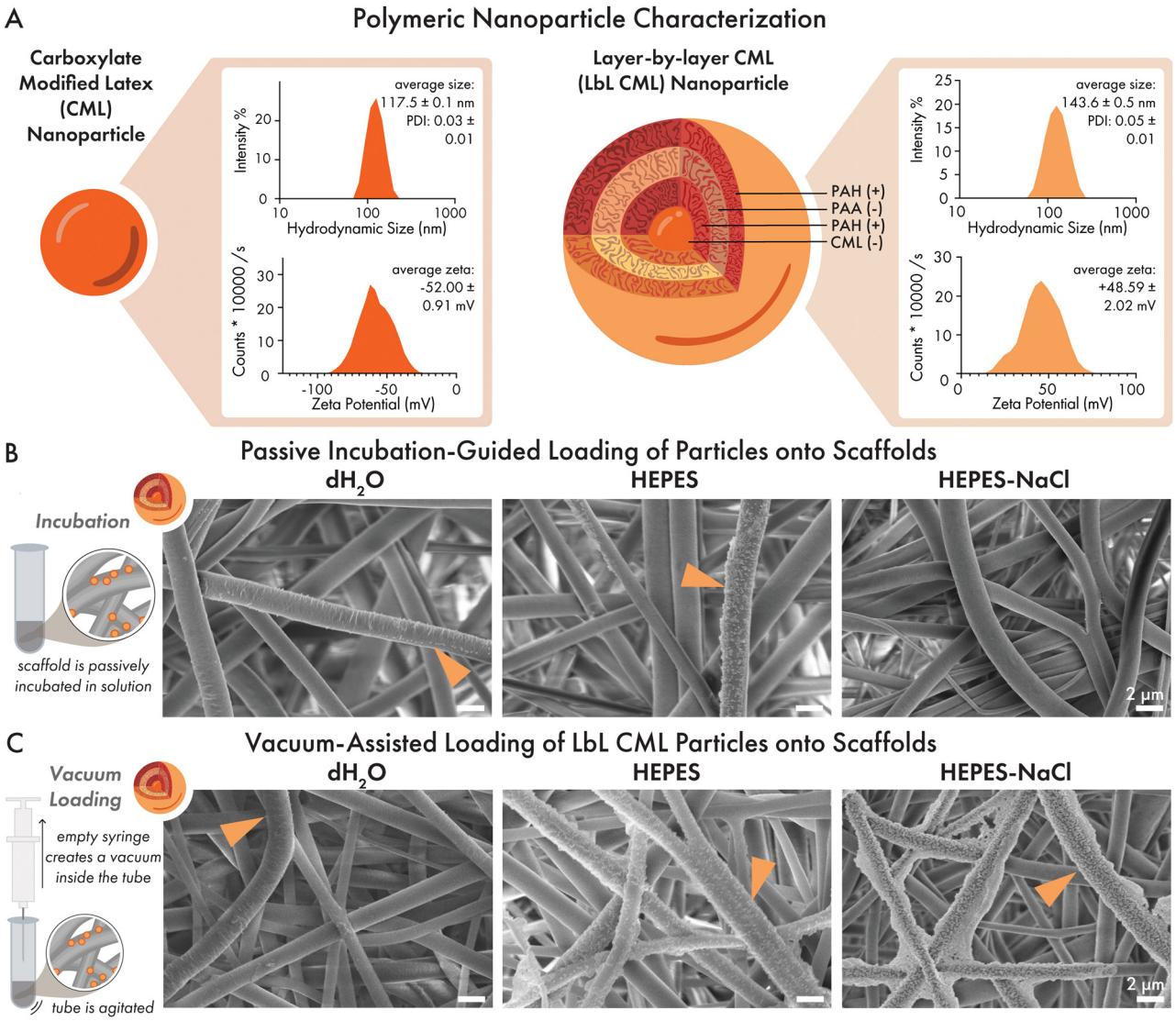

Fig. 1 Systematic comparison of loading methodology on charged particles reveals optimal loading technique: (A) carboxylate modified latex (CML) particle (left) and layer-by-layer CML particles (LbL CML, right). Hydrodynamic size and zeta potential were characterized with dynamic light scattering; values are reported as mean ± SEM with n = 3 replicates. (B) Scanning electron microscopy images of particle coatings with incubation-guided loading on poled scaffolds in deionized water (left), HEPES buffer (middle), or HEPES buffer + NaCl (right) with LbL CML NPs at 2 mg mL^{-1}. (C) Scanning electron microscopy images of particle coatings with vacuum-assisted loading in deionized water (left), HEPES buffer (middle), or HEPES buffer + NaCl (right) with LbL CML NPs at 2 mg mL^{-1}. Arrows indicate discrete particles and/or particle plaques.

influence scaffold coating outcomes. Each was tested on poled scaffolds at two nanoparticle concentrations (0.5 and 2 mg mL^{-1}), alongside vacuum-loaded buffer-only controls.

SEM revealed that under vacuum-assisted loading, scaffolds treated in deionized water displayed sparse nanoparticle coatings, consistent with our earlier observations. Morphological improvements were observed under buffered conditions: HEPES led to moderate, plaque-like adsorption, while HEPES supplemented with NaCl yielded the most uniform and dense surface coverage (Fig. 1C). These findings indicate that optimal adsorption required simultaneous tuning of both pH and ionic strength to support charge stability and minimize repulsive interactions. However, in the passive incubation condition, modest nanoparticle coverage was observed when loading in HEPES buffer alone, but little to no coverage occurred in HEPES supplemented with NaCl (Fig. 1B). We speculate that under passive incubation, the surface charge of the poled scaffold fibers is relatively low, such that the addition of salt leads to substantial electrostatic screening and prevents nanoparticle–scaffold interactions. In contrast, during vacuum-assisted loading, mechanical deformation of the piezoelectric PVDF-TrFE fibers likely generates surface charge, enabling short-range electrostatic attraction to dominate even in the presence of elevated ionic strength. Under these conditions, ionic screening may instead reduce interparticle repulsion, promoting more uniform, dense adsorption.

We next compared the effect of particle charge on adsorption. Notably, particle adsorption was observed for both cationic and anionic nanoparticles (Fig. 2A and B), heterogeneously coating fibers throughout the scaffold (SI Fig. 3 and 4). This suggests that the bulk poled scaffold generates heterogeneous surface potentials during mechanical deformation, with coexisting domains of positive and negative charge. This is consistent with prior studies demonstrating strain gradients in piezoelectric polymers, particularly in thin and flexible materials, that can produce spatially patterned electric fields.[54] Several groups have leveraged this behavior to guide polymer adsorption or create self-patterned materials using electrostatic self-assembly principles.[55–57]

Together, these results introduce a strategy for noncovalent, post-fabrication functionalization of piezoelectric scaffolds with nanotechnology. This is significant for tissue engineering applications, where electrospun fibers are commonly used as extracellular matrix (ECM) mimics.[26,58] While strategies such as physical adsorption or encapsulation of proteins and small molecules,[59–62] blend electrospinning of polymers with bioactive agents,[30,63–65] coaxial electrospinning for core–shell architectures,[66–68] and covalent immobilization of ligands or growth factors[69–71] have been used to functionalize scaffolds, they often involve harsh processing, irreversible chemistry, or limited modularity.[72] In contrast, our electrostatic adsorption method circumvents many of these issues by enabling post-fabrication scaffold modification under mild conditions, with tunable coating density using either cationic or anionic nanoparticles. This renders our technique particularly well-suited for presenting fragile or multi-component nanocarriers and supports its utility in modular regenerative medicine platforms.

Evaluating the effect of scaffold poling on nanoparticle adsorption

Given the role of substrate surface charge in electrostatic adsorption, we next asked whether corona poling of the scaffold is required for efficient polymeric nanoparticle adsorption, or whether optimized solution conditions and mechanical deformation during vacuum-assisted loading are sufficient. Although PVDF-TrFE electrospun scaffolds can be poled to enhance surface charge upon mechanical deformation, poling is time-intensive and difficult to scale, motivating us to evaluate whether this step is necessary.

To evaluate the necessity of poling for nanoparticle adsorption, we coated both poled and unpoled scaffolds with fluorescent CML nanoparticles under three buffer conditions (Fig. 3A) and quantified surface fluorescence. Across both nanoparticle concentrations (0.5 mg mL^{-1} and 2 mg mL^{-1}), buffer composition strongly influenced coating efficiency, while poling had minimal effect. In deionized water, the mean nanoparticle adsorption was minimal for both poled and unpoled scaffold types at 0.5 mg mL^{-1} (1.73 *vs.* 2.60 RFU μm^{-2}; $p > 0.99$) and at 2 mg mL^{-1} (1.72 *vs.* 0.73 RFU

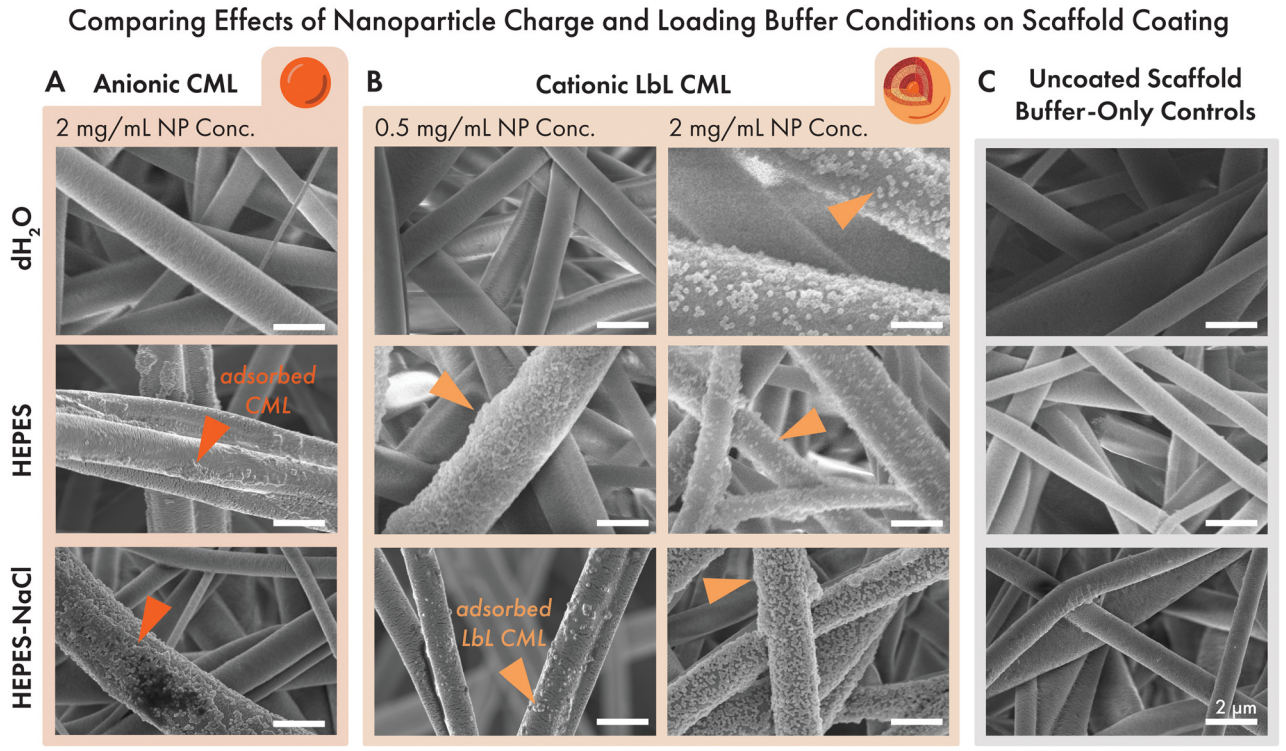

Fig. 2 Solution conditions tune nanoparticle loading onto scaffolds. Scanning electron microscopy images of particle coatings at different densities (0.5 mg mL^{-1} and 2 mg mL^{-1}) and in different loading buffers (dH_2O, HEPES, HEPES-NaCl (top to bottom)) on poled scaffolds: (A) CML, (B) LbL CML, and (C) no particles. Arrows indicate discrete particles and/or particle plaques. Scale bar = 2 µm and is applicable to all images.

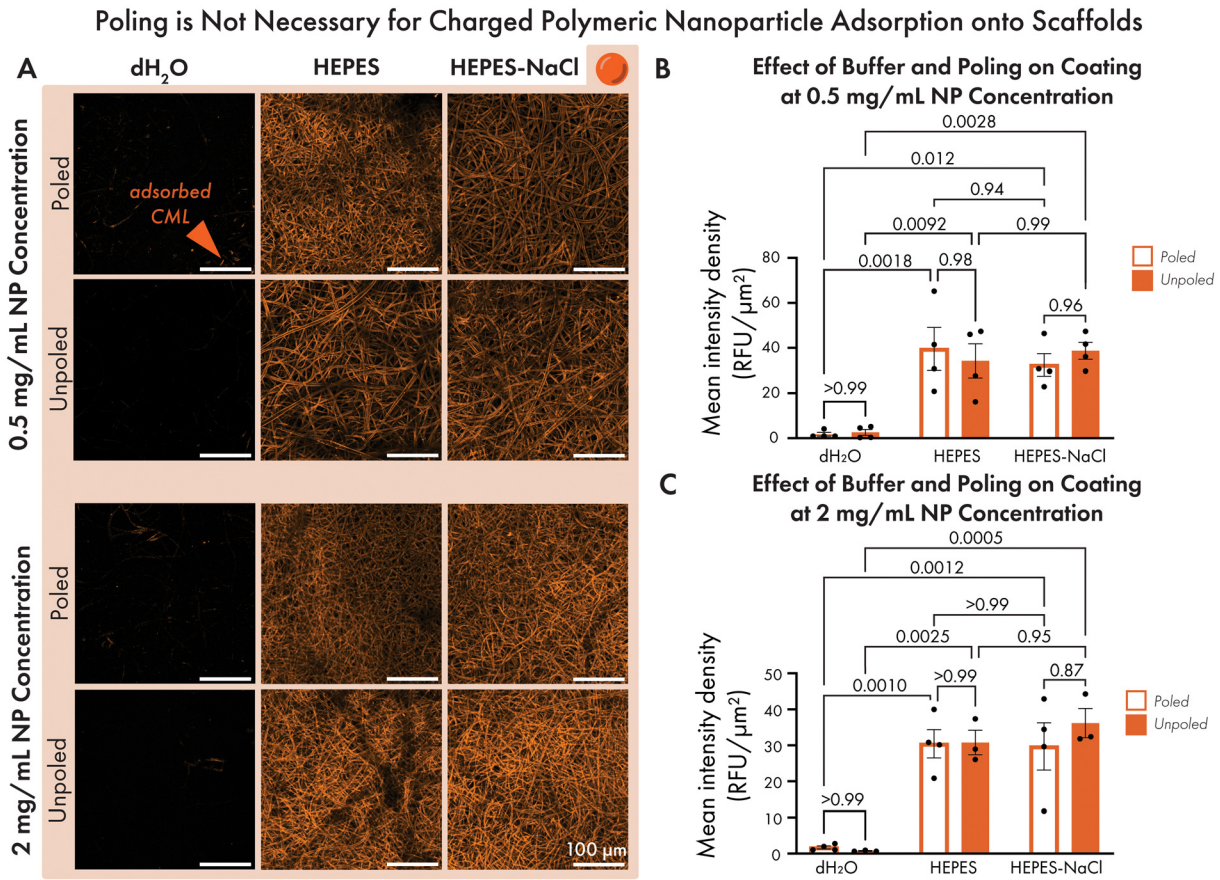

Fig. 3 Comparing the effect of scaffold poling on nanoparticle adsorption. (A) Confocal microscopy of 50 µm *Z*-stack maximum intensity projections of vacuum-loaded adsorbed anionic CML NPs on unpoled and poled scaffolds at different densities (0.5 mg mL^{-1} (top) and 2 mg mL^{-1} (bottom)) in dH_2O, HEPES, and HEPES-NaCl (left to right), scale bar = 100 µm and is applicable to all images; image-based quantification of mean fluorescence intensity of scaffolds coated with (B) 0.5 mg mL^{-1} or (C) 2 mg mL^{-1} CMLs with n = 3–4 scaffolds/condition. Two-way ANOVA is followed by Tukey's multiple comparisons test. Values are represented as mean ± SEM.

μm^{-2}; $p > 0.99$). In HEPES, poled and unpoled scaffolds exhibited comparable coatings at 0.5 mg mL^{-1} (39.59 *vs.* 34.32 RFU μm^{-2}; $p = 0.98$) and at 2 mg mL^{-1} (30.44 *vs.* 30.79 RFU μm^{-2}; $p > 0.99$). In HEPES-NaCl, adsorption was similarly strong and uniform at 0.5 mg mL^{-1} (32.44 *vs.* 38.76 RFU μm^{-2}; $p = 0.96$) and at 2 mg mL^{-1} (29.69 *vs.* 36.16 RFU μm^{-2}; $p = 0.87$). These results confirm that efficient and uniform nanoparticle adsorption can be achieved without the need for scaffold poling, provided appropriate pH and ionic strength are used (Fig. 3B and C).

Nanoparticle adsorption was strongly influenced by buffer composition, with both coating efficiency and consistency improved by tuning pH and ionic strength. At 0.5 mg mL^{-1}, mean fluorescence intensity was minimal in deionized water for both poled and unpoled scaffolds. While mean adsorption on poled and unpoled scaffolds was significantly enhanced in HEPES and HEPES-NaCl, there was no significant difference between the two conditions in terms of mean intensity. However, the inclusion of NaCl improved coating uniformity: the coefficient of variation (CV) at 0.5 mg mL^{-1} was lower in HEPES-NaCl than in HEPES for both poled (30.62% *vs.* 48.12%) and unpoled (19.41% *vs.* 43.92%) scaffolds, and markedly higher variability was observed in deionized water (94.80% poled, 100.63% unpoled) (SI Fig. 5 and 6). Further increasing the CML nanoparticle concentration to 2 mg mL^{-1} did not appreciably improve surface coverage, suggesting that scaffolds were approaching saturation at 0.5 mg mL^{-1} (SI Fig. 7). Follow-up experiments revealed that saturation occurs between 0.1 and 0.5 mg mL^{-1} in HEPES and HEPES-NaCl (SI Fig. 8). However, the use of higher nanoparticle concentration also reduced the CV, suggesting that an excess of nanoparticle can promote more uniform coatings.

Overall, these findings suggest that under optimal buffer conditions, the induced polarization generated by mechanical deformation during vacuum-assisted loading is sufficient to support robust nanoparticle adsorption. This result suggests that poling of the PVDF-TrFE electrospun scaffold is not a prerequisite for electrostatic adsorption of charged nanoparticles, establishing a simplified and scalable design rule allowing for a more efficient processing pipeline.

Extending nanomaterial coatings to liposomal nanotechnology

To adapt our nanoparticle coating platform for the delivery of biologically active signals, we selected liposomes as a modular and clinically relevant nanocarrier. Liposomes are biocompatible vesicles that can encapsulate small molecules within their bilayer or aqueous core, and their surfaces can be engineered to display proteins, lipids, or targeting ligands.[35,73–75] Their surface chemistry, including overall charge, can be readily tuned by selecting different phospholipids and lipid components.[76] Based on our results with polymeric nanoparticles, we hypothesized that charged liposomes could similarly adsorb to the scaffold under optimized buffer conditions. To validate this, we selected a cationic liposome formulation consisting of 1,2-distearoyl-*sn-glycero*-3-phosphocholine (DSPC), 1,2-dioleoyl-3-trimethylammonium-propane (DOTAP), and plant cholesterol, used at a 9 : 1 : 2 molar ratio, which we have previously used with liposomal biomaterials for drug delivery.[75] We synthesized unilamellar liposomes with a mean diameter of 159.9 ± 0.3 nm, a low polydispersity index (0.05 ± 0.02), and a zeta potential of +50.75 ± 0.91 mV, indicating a stable, highly charged nanoparticle suitable for electrostatic self-assembly[35,77] (Scheme 1, SI Fig. 1).

To determine whether the design rules identified for polymeric nanoparticle adsorption extend to lipid-based nanocarriers, we evaluated the effects of buffer composition, liposome concentration, and scaffold poling on liposome adsorption. Fluorescently labeled liposomes were adsorbed onto poled PVDF-TrFE scaffolds using vacuum-assisted loading in three buffer conditions: dH_2O, HEPES buffer (500 mM, pH = 7.5), and HEPES (500 mM, pH = 7.5) further supplemented with NaCl (400 mM).

Across both liposome concentrations tested (0.5 mg mL^{-1} and 2 mg mL^{-1}), buffer composition was the dominant determinant of adsorption efficiency and uniformity. On poled scaffolds, dense and uniform liposome coatings were observed in HEPES and HEPES-NaCl at 0.5 mg mL^{-1} (8.64 and 10.01 RFU μm^{-2}) and at 2 mg mL^{-1} (18.07 and 19.40 RFU μm^{-2}). In contrast, coatings formed in deionized water were sparse and heterogeneous at 0.5 mg mL^{-1} (1.29 RFU μm^{-2}) but much denser at 2 mg mL^{-1} (28.67 RFU μm^{-2}) (Fig. 4A and B). Unlike with the CML nanoparticles, we did not observe saturation of the scaffold surface (SI Fig. 7, SI Table 1). When using dH_2O, we also observed a punctate morphology of the liposome coating, which may indicate aggregation of the liposomes using unbuffered conditions. As with polymeric nanoparticles, the reproducibility of liposomal coatings, assessed by CV, also improved with HEPES-NaCl (SI Fig. 6 and 9): at 0.5 mg mL^{-1}, CV was 1.76% in dH_2O, 140.26% in HEPES, and 25.49% in HEPES-NaCl. These results indicate that pH stabilization and moderate ionic strength enable improved and more replicable adsorption, consistent with electrostatic self-assembly principles.

We next examined whether scaffold poling was required for liposome adsorption under optimized buffer conditions at the higher 2 mg mL^{-1} liposome concentration. In dH_2O, adsorption occurred only on poled scaffolds (28.67 RFU μm^{-2} on poled *vs.* 0.32 RFU μm^{-2} on unpoled; $p = 0.013$), indicating that poling is required under low-ionic-strength conditions. In contrast, in HEPES and HEPES-NaCl, unpoled scaffolds exhibited improved adsorption comparable to poled counterparts. In HEPES, mean intensities were 18.07 RFU μm^{-2} (poled) *vs.* 32.79 RFU μm^{-2} (unpoled) ($p = 0.029$), and in HEPES-NaCl, 19.40 RFU μm^{-2} (poled) *vs.* 35.54 RFU μm^{-2} (unpoled) ($p = 0.11$). Moreover, unpoled scaffolds in HEPES-NaCl and HEPES exhibited lower CVs (3.37% and 1.88%, respectively) *vs.* 105.6% in dH_2O (SI Fig. 6). Poled scaffolds also exhibited punctate morphologies when using dH_2O or HEPES-NaCl, which may indicate aggregation of the liposomes, whereas unpoled scaffolds exhibited more uniform coatings. To orthogonally verify liposome adsorption under our optimized conditions, we performed energy-dispersive X-ray spectroscopy (EDS) on unpoled scaffolds coated with 2 mg mL^{-1} liposomes in HEPES-NaCl (Fig. 4C). Nitrogen content increased signifi-

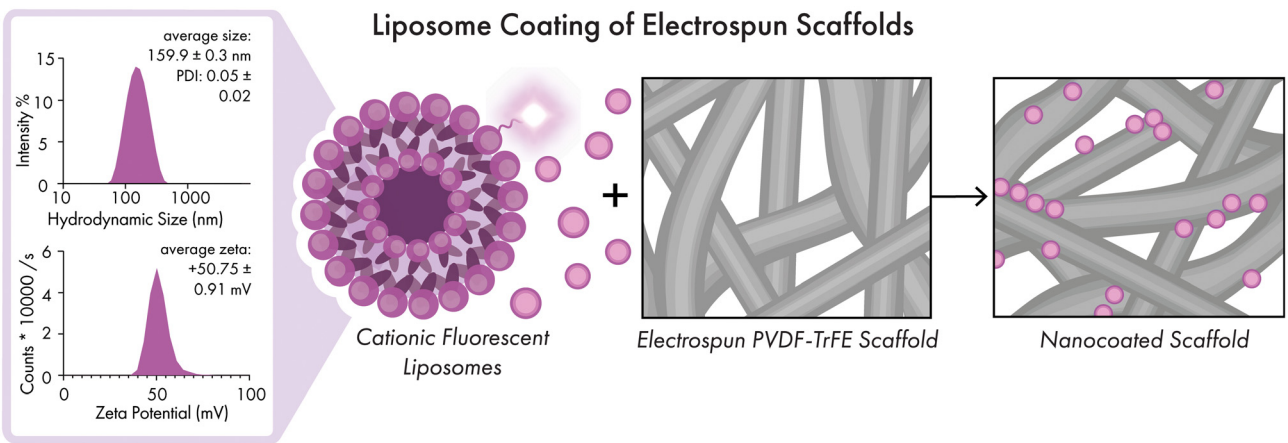

Scheme 1 Electrostatic liposome adsorption onto PVDF-TrFE scaffolds, hydrodynamic size and zeta potential of liposomes was characterized with dynamic light scattering with $n = 3$ replicates. Summary values are represented as mean ± SD.

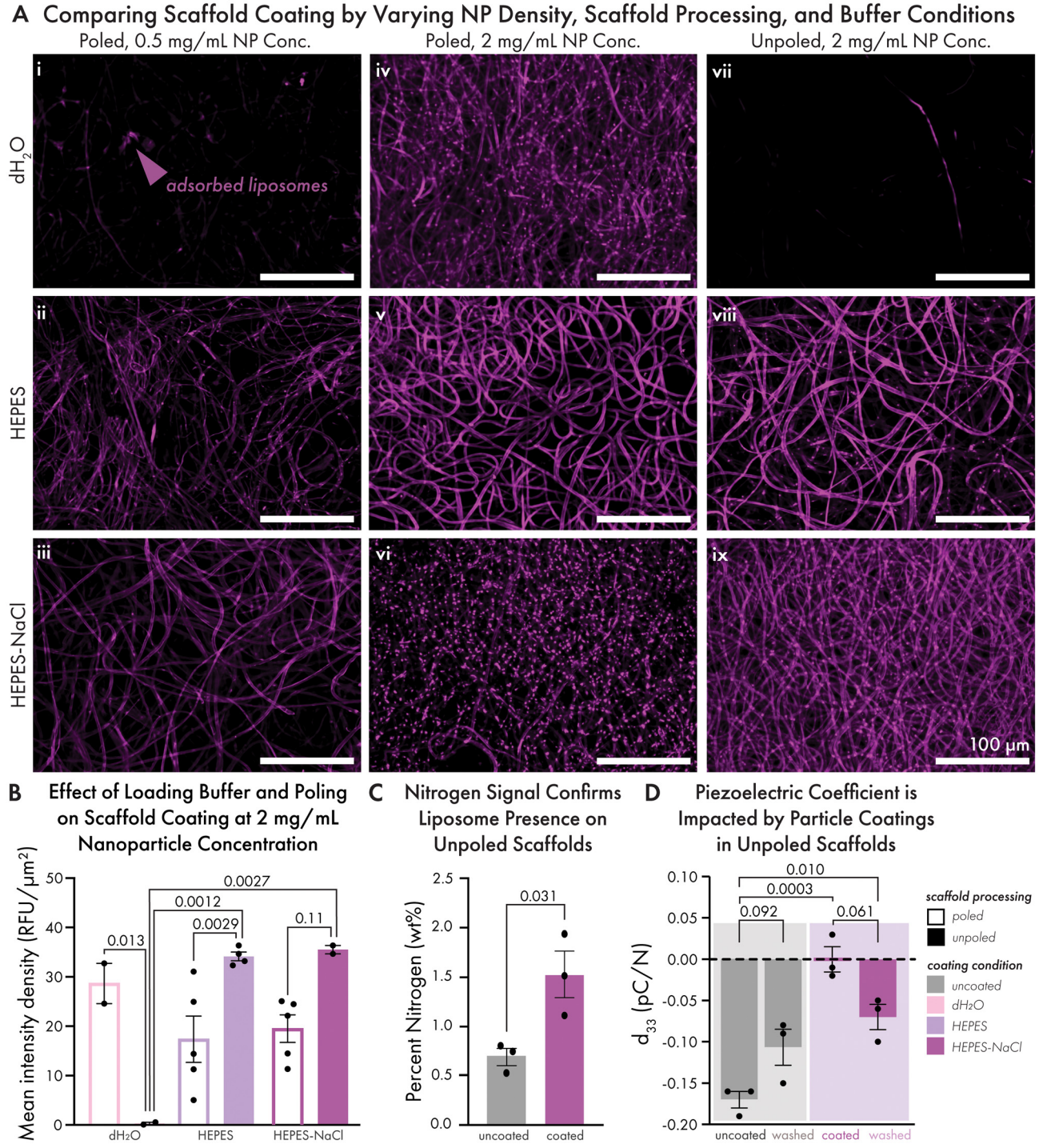

Fig. 4 Electrostatic liposome adsorption onto PVDF-TrFE scaffolds: (A) fluorescence microscopy of Cy5 labeled liposomes on scaffolds coated in deionized water, HEPES, and HEPES-NaCl (top to bottom) at low NP concentration (0.5 mg mL^{-1}) or high NP concentration (2 mg mL^{-1}) on poled scaffolds, or high NP concentration on unpoled scaffolds (left to right); scale bar = 100 µm and is applied to all groups. Images are collected at the same laser power and are contrast-matched using Fiji-ImageJ. (B) Image-based quantification of liposome adsorption onto scaffolds. (C) Energy-dispersive X-ray spectroscopy measurements of nitrogen levels on unpoled scaffolds coated with 2 mg mL^{-1} of liposomes in HEPES-NaCl, (D) piezoelectric coefficient, d_{33}, on unpoled scaffolds, uncoated or coated with 2 mg mL^{-1} of liposomes in HEPES-NaCl, pre- and post-ethanol wash. All values are represented as mean ± SEM and pair-wise statistics are performed using Student's paired *t*-tests. Multiple comparisons following two-way ANOVA for image-based fluorescence quantification and d_{33} measurements are corrected by Tukey's multiple comparisons test.

cantly from 0.692 ± 0.107% (uncoated) to 1.522 ± 0.291% (coated) (p = 0.0308), consistent with the presence of nitrogen-bearing DSPC and DOTAP lipids in the liposomes. Overall, these data indicate that the combination of unpoled surfaces and appropriate buffer conditions mediate more reproducible liposomal coatings.

Next, we assessed whether nanoparticle coatings altered the intrinsic piezoelectric properties of the scaffold. We measured the piezoelectric coefficient (d_{33}) of unpoled PVDF-TrFE scaffolds before and after coating with cationic liposomes. Liposome-coated scaffolds showed a significant reduction in d_{33} values, decreasing in magnitude from −0.17 ± 0.01 pC N^{-1} in uncoated scaffolds to 0.00 ± 0.02 pC N^{-1} after coating (p = 0.0003; Fig. 4D). A similar attenuation was observed with polymeric nanoparticle coatings (SI Fig. 10), suggesting that surface-bound nanoparticles broadly influence measured piezoelectric behavior. To determine whether this effect reflects a reversible phenomenon due to the coating or a lasting change to scaffold properties, we removed liposomes with ethanol and re-measured d_{33}. Ethanol-washed scaffolds showed partial recovery of piezoelectric response (−0.07 ± 0.02 pC N^{-1}), representing a large effect size compared to PBS-washed controls (Cohen's d = 2.65), although the difference did not reach statistical significance (p = 0.06). Notably, ethanol washing also reduced d_{33} in uncoated scaffolds, suggesting that the observed recovery may underestimate the true reversibility of the effect. Taken together, these findings support a model in which nanoparticle coatings attenuate piezoelectric output *via* interfacial dielectric effects, without permanently altering scaffold polarization.

Lastly, to assess whether liposome morphology was maintained during adsorption, we characterized particles that were passively desorbed in phosphate-buffered saline (PBS) using dynamic light scattering and zeta potential analysis. Liposomes retained similar size (172.55 ± 4.80 nm *vs.* 128.4 ± 2.06 nm pre-adsorption; p < 0.0001), PDI (0.16 ± 0.06 *vs.* 0.099 ± 0.02), and zeta potential (58.81 ± 1.51 mV *vs.* 58.15 ± 0.41 mV; p = 0.88) (SI Fig. 11). The increase in size is consistent with reported size changes in liposomes stored in aqueous solutions.[78] These findings suggest that the liposomes remain as discrete nanoparticles following adsorption.

While our results establish a reliable strategy for liposome adsorption, several questions remain regarding how scaffold and particle properties interact at the interface. In particular, poled scaffolds appear to have a more complex interaction with liposomes, which, unlike polymeric nanoparticles, can mediate adsorption in less favorable, unbuffered conditions but also appears to contribute to morphological irregularities. Given these findings, our subsequent studies exclusively focus on liposome coatings on unpoled scaffolds (SI Table 2).

Assessing biocompatibility and immune cell engagement with liposome-coated scaffolds

We next set out to determine if cationic liposome coated scaffolds could be used for 3D cell culture. PVDF-TrFE is a synthetic, non-degradable polymer that is intrinsically hydrophobic, with a reported water contact angle of 134.3 ± 4.3°.[30] Unmodified PVDF-TrFE scaffolds have been widely used for tissue engineering,[30,79–81] but the introduction of cationic nanoparticle coatings introduces questions of coating stability and new interfaces that may influence both cell viability and behavior.

To assess the stability of liposome coatings under aqueous conditions relevant to cell culture, we quantified the release of fluorescent lipids from fluorescent liposome-coated scaffolds over time. Lipid release in aqueous solution (PBS) was compared to release in ethanol, which served as positive control for complete particle solubilization. While the majority of fluorescent lipids were rapidly released into ethanol within 24 hours, with near-complete release by 48 hours, minimal lipid release was detected in PBS for up to 192 hours of incubation, indicating sustained retention of liposomes on the scaffold in aqueous conditions (SI Fig. 12).

We next assessed cytocompatibility and cell engagement of liposome-coated scaffolds using both adherent and suspension cell models: HEK293 cells were used as a standard model for assessing general cytocompatibility, and Jurkat T cells were used to explore the potential of this platform for *ex vivo* immune cell culture. HEK293 cells were cultured on uncoated or cationic liposome-coated unpoled PVDF-TrFE scaffolds for eight days in low-adherence culture plates to promote scaffold seeding. Cell viability was quantified using the CCK8 assay, which measures metabolic activity *via* WST-8 reduction. HEK293 cells remained viable throughout the culture period, with no significant difference in metabolic activity between coated and uncoated scaffolds (p = 0.2300; Fig. 5A). Jurkat T cells also remained viable when cultured on unpoled liposome-coated scaffolds, as confirmed by calcein-AM staining after three days in culture (Fig. 5B).

To evaluate cell–material engagement, we examined cytoskeletal organization and assessed whether components of the liposome coating were transferred to the cell membrane. Jurkat T cells seeded onto Cy5-labeled liposome-coated scaffolds were fixed and stained for F-actin and DAPI on day four of cell culture. Confocal microscopy revealed that cells were adhered to scaffold fibers and exhibited a cortical actin distribution, with occasional actin-rich puncta at points of fiber contact (Fig. 5C). In addition, Cy5-labeled lipids from the scaffold coating were visible within the plasma membranes of Jurkat T cells (Fig. 5C, panels i,ii). This membrane-associated signal suggests that cells actively engage with and take up components of the scaffold's liposome coating.

Our findings indicate that adding a cationic liposome coating preserves PVDF-TrFE scaffold biocompatibility while introducing a means for tunable nanomaterial presentation. Jurkat T cell behavior on these scaffolds was consistent with typical behaviors of immune cells interacting with three-dimensional substrates,[82] despite the inherently hydrophobic nature of PVDF-TrFE. Moreover, the incorporation of Cy5-labeled lipids into the cell membrane indicates active transfer of nanomaterials from the scaffold to cells, potentially through lipid exchange or membrane fusion.[83,84]

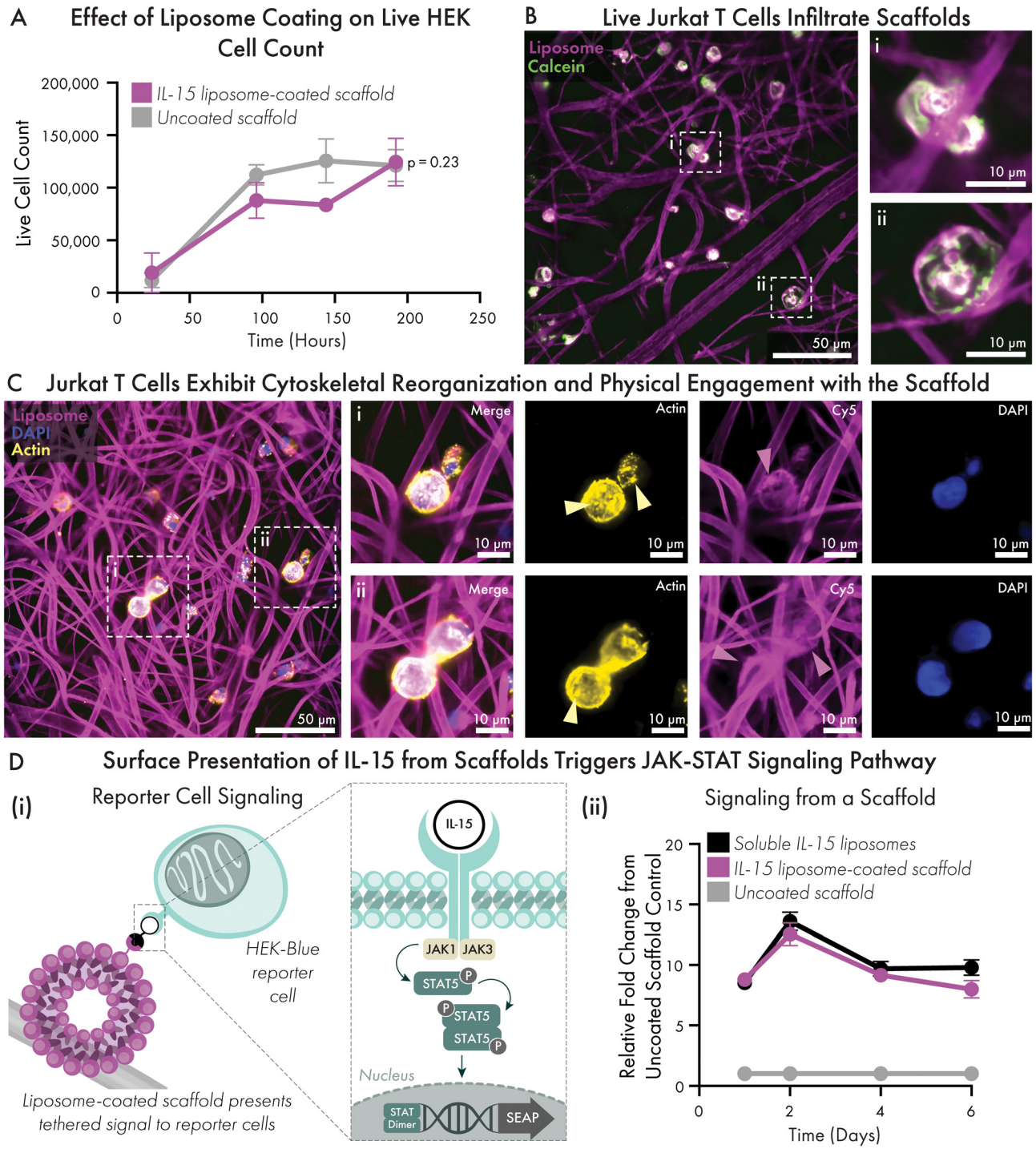

Fig. 5 Liposome coated scaffolds are suitable substrates for cells and enable cytokine presentation: (A) live HEK293 cell counts were measured from multiple time points on unpoled scaffolds with and without cationic liposome coating. Data is presented as mean ± SEM from 3 independent wells at each time point. Statistical significance was assessed by two-way ANOVA with Sidak's multiple comparisons test, comparing coated to uncoated scaffold at each time point. *P* values reflect differences between groups at individual time points, and all error bars are present on graph although some are too small to see. (B) Unpoled scaffolds were coated with fluorescent Cy5-labeled liposomes and imaged with confocal microscopy. Jurkat T cells were stained with calcein, cultured on Cy5 liposome-coated scaffolds, and imaged at 60× resolution 3 days after plating. (C) Jurkat T cells were fixed on day 4 and stained intracellularly with ActinProbe555 and DAPI. Arrows indicate punctate actin (yellow) or liposome uptake (magenta). Scale bars are 50 μm or 10 μm. (D) Activating the JAK-STAT Pathway with IL-15 Liposomes on Scaffolds: (i) unpoled scaffolds were coated with 2 mg mL^{-1} of IL-15-tethered liposomes in optimized HEPES-NaCl buffer conditions and SEAP is produced in response to IL-15 recognition. (ii) IL-15 reporter cells were plated on unpoled scaffolds, and absorbance was read daily, correlating to the downstream SEAP production from activation of the JAK-STAT pathway with n = 3 samples per group. Data is presented as relative fold change from uncoated scaffold control, with mean ± SD. Significance is conducted with an Ordinary Two-Way Anova with multiple comparisons using Šídák's multiple comparisons test.

Demonstrating surface presentation of IL-15 cytokine from scaffolds to support functional JAK-STAT signaling

Having established that liposome-coated scaffolds support cell viability, we next investigated whether the scaffold interface could locally present functional signaling proteins in a surface-bound configuration. In contrast to soluble cytokine delivery, which is often limited by the cytokine's rapid diffusion, degradation, and off-target effects, surface-tethered presentation enables more stable and spatially confined signal delivery.[85] We have previously used histidine–nickel affinity interactions to tether recombinant cytokines to liposome surfaces in hydrogel systems,[75] and we hypothesized that this supramolecular approach could be extended to liposomes adsorbed onto PVDF-TrFE scaffolds. To test this, we focused on interleukin-15 (IL-15), a cytokine of interest for *ex vivo* immune cell culture[86] due to its role in promoting the survival and expansion of memory CD8+ T cells and NK cells.[10,87,88]

To tether IL-15 to the scaffold, we incorporated 0.379 mol%[75] of the nickel-chelating lipid DGS-NTA(Ni) into the liposome bilayer and adsorbed the functionalized liposomes onto unpoled PVDF-TrFE scaffolds using the optimized vacuum-assisted loading protocol with HEPES-NaCl loading buffer. His-tagged recombinant IL-15 was bound to the liposomes *via* overnight incubation prior to coating liposomes onto scaffolds. To assess IL-15 bioactivity, we used IL-15-responsive HEK293 reporter cells (HEK-Blue CD122/132) which secrete alkaline phosphatase (SEAP) in response to IL-15 receptor mediated phosphorylation of STAT5 (Fig. 5D i). Reporter cells were seeded directly onto scaffolds in a non-tissue culture-treated plate to encourage cell-scaffold integration, and SEAP levels were independently measured over the course of six days. We compared IL-15 liposome-functionalized scaffolds, uncoated scaffolds with soluble IL-15, and uncoated scaffolds without cytokine. STAT-5 phosphorylation increased similarly between cells cultured on scaffolds with soluble IL-15 as on scaffolds presenting liposome-bound IL-15 for days 1, 2, and 4 ($p = 0.9814$, $p = 0.2453$, $p = 0.8108$, respectively) and only a moderate decrease in intensity was noted on day 6 (81.56% relative to soluble, $p = 0.0167$) (Fig. 5D ii). This reduction likely reflects minor IL-15 loss during coating, as the soluble control corresponded to 100% theoretical scaffold loading (0.477 μM IL-15).

These results confirm that scaffold-tethered IL-15 remains bioactive and capable of engaging cell surface receptors. More broadly, they demonstrate that liposome-coated scaffolds provide a modular platform for spatially confined cytokine presentation. By displaying IL-15 at the scaffold surface through supramolecular tethering, we preserved cytokine function and achieved localized receptor-mediated signaling without requiring covalent modification of either the cytokine or the scaffold. This flexible strategy enables the facile incorporation of his-tagged proteins into electrospun materials and may prove particularly valuable for *ex vivo* immune cell expansion and reprogramming.

Conclusion

This work establishes a modular strategy for post-fabrication functionalization of piezoelectric electrospun scaffolds using electrostatically adsorbed nanocarriers. By combining vacuum-assisted loading with buffer-optimized solution conditions, we enable stable adsorption of charged nanoparticles, including both polymeric and lipid nanoparticles, onto PVDF-TrFE scaffolds. We applied this modular platform to a biomedically relevant context by generating scaffolds coated with liposomes decorated with immunomodulatory cytokines. These nanocoated scaffolds supported cell viability, enabled lipid exchange between immune cells and scaffold-bound liposomes, and activated cellular signaling pathways. Together, these findings demonstrate that the platform supports localized cytokine presentation and highlight its potential as an immune-instructive biomaterial in applications such as *ex vivo* cell engineering and 3D cell culture.

While this platform shows strong potential for modular signal presentation, several limitations remain that point to opportunities for future research. The modular nature of this system invites the presentation of other his-tagged proteins, and future studies will be conducted to explore the ability to present multiple protein cues. Further, the ability to tether IL-15 to the scaffold surface and trigger localized signaling suggests this system could support immune-instructive cues in *ex vivo* or therapeutic settings. However, we evaluated cytokine activity using a HEK293-based reporter line, and it remains to be determined whether the platform can drive similar or enhanced responses in primary immune cells such as T or NK cells.

Looking ahead, this electrostatic coating strategy could be extended to a broad range of surface-charged nanocarriers, including extracellular vesicles, polymeric micelles, hybrid nanoparticles, and solid lipid nanoparticles (LNPs). Incorporating LNPs would enable scaffold-tethered gene delivery, combining nucleic acid cargo with the structural and biophysical advantages of electrospun materials. The use of liposomes as a modular display vehicle also opens opportunities for multivalent or combinatorial presentation of proteins, such as co-delivered cytokines, chemokines, and growth factors. More broadly, the ability to tune surface coverage through buffer composition and nanoparticle concentration offers a simple and scalable method for customizing scaffold interfaces. Together, these features position this approach as a flexible foundation for engineering multifunctional, cell-responsive scaffolds with potential applications in regenerative medicine, immune engineering, and *ex vivo* cell culture.

Materials and methods

PVDF-TrFE scaffold fabrication

Scaffolds were electrospun following previously reported methods[47,79] with several modifications. Briefly, 20% (w/v) solutions of poly(vinylidene fluoride tri-fluoroethylene) (PVDF-TrFE, 70/30) (400 kDa, poly-dispersity index (PDI) of 2.1, Solvay Solexis Inc., Thorofare, NJ) in 2-butanone/methyl ethyl ketone (Sigma-Aldrich # 360473) were filled into a 10 mL

syringe and extruded though an 18-gauge needle, with a 3 ml per hour flow rate. A voltage of 22 kV was connected to the needle tip and randomly oriented fibers were collected on a grounded metal collector plate placed 22–24 cm apart from the needle tip. The fibers were spun at room temperature (~20 °C) with 20–30% humidity followed by aerating the electrospun fibrous mat for at least 48 hours. The scaffolds were annealed at 135 °C for 96 hours and quenched as described in previous methods.[30]

Corona poling. The scaffolds were corona poled using a custom setup described previously.[47] Briefly, the scaffolds were heated to a temperature of approximately 47 °C for 3 hours on a grounded heating plate. A metal grid connected to a primary voltage source (set at 2 kV) was set 2 cm above the scaffolds. A needle connected to a secondary voltage source (set at 14 kV) was placed above the grid with the needle tip oriented in the direction of the grid.

Scaffold fiber diameter measurements. A total of 40 fibers from different spots of 5 distinct SEM images were quantified using Fiji-Image J for each scaffold processing group.

Layer-by-layer nanoparticle synthesis

100 nm carboxyl-modified latex nanoparticles (CML) (ThermoFisher Scientific #F8801) were coated in three layers of poly-allylamine hydrochloride (PAH) (Sigma-Aldrich #283215), poly(acrylic acid, sodium salt) solution (PAA) (Sigma-Aldrich # 416029) and PAH. PAH was prepared at 4 mg mL^{-1} and 6 mg mL^{-1} in MilliQ water. PAA was prepared at 4 mg mL^{-1} in MilliQ water. CML were prepared at 1 mg mL^{-1} and combined with equal volume of PAH. The solution was pipetted in a bath sonicator three times. The particles were spun at 25 830*g* for 45 minutes at 4 °C. The supernatant was removed, and 0.8 times the original particle volume minus the particle volume remaining of MilliQ water was added to the solution to resuspend the particles. Equal volume of 4 mg mL^{-1} PAA was added to the particle solution by pipetting inside a bath sonicator. The particles were spun at 25 830*g* for 45 minutes at 4 °C. The supernatant was again removed, and 0.8 times the original particle volume minus the particle volume remaining of MilliQ water was added to the solution to resuspend the particles. Equal volume of 6 mg mL^{-1} PAH was added to the particle solution by pipetting inside a bath sonicator. The particles were spun at 25 830*g* for 45 minutes at 4 °C. The supernatant was removed, and the particles were resuspended in loading buffer.

Liposome synthesis

Liposomes were prepared using the thin-film rehydration technique. 1,2-Distearoyl-*sn-glycero*-3-phosphocholine (18:0 PC (DSPC)) (Avanti Polar Lipids #850365), 1,2-dioleoyl-3-trimethylammonium-propane (chloride salt) (18:1 TAP (DOTAP)), (Avanti Polar Lipids #890890), cholesterol (plant) (Avanti Polar Lipids #700100), and 1,2-dioleoyl-*sn-glycero*-3-[(*N*-(5-amino-1-carboxypentyl)iminodiacetic acid)succinyl] (nickel salt) (18:1 DGS-NTA(Ni)) (Avanti Polar Lipids #790404) were dissolved at a 9 : 1 : 2 : 0.379 molar ratio in chloroform. Solvent was removed by evaporation under vacuum using a rotovap with water bath temperature at 65 °C. The thin film was rehydrated at the desired concentration in loading buffer in a bath sonicator at 60 °C for 30 min. For fluorescent liposomes only, 1,2-distearoyl-*sn-glycero*-3-phosphoethanolamine-*N*-(Cyanine 5) fluorescent lipid (18:0 Cy5 PE) (Avanti Polar Lipids #810345) was added at 0.01 mol% during sonication. Liposomes were extruded at 60 °C (Avanti Research #610000) using 10 mm filter supports (Avanti Polar Lipids #610014) through PC 1.0 μm membrane (Avanti Research #610010), PC 0.4 μm membrane (Avanti Research #610007), PC 0.2 μm membrane (Avanti Research #610006) and PC 0.1 μm membrane (Avanti Research #610005).

Nanoparticle characterization

Nanoparticle hydrodynamic size and polydispersity index were measured using dynamic light scattering (Malvern Zetasizer Advanced Pro Red), λ = 633 nm, dispersant RI = 1.33. Zeta potential measurements were also acquired with the Malvern Zetasizer, using laser Doppler electrophoresis. Nanoparticles were diluted 1 : 1000 in Milli-Q water, with no added salts, in polystyrene Greiner Bio-One Semi-micro/Macro cuvettes (Fisher Scientific #07-000-571) or Folded Capillary Zeta Cell (Malvern Paranalytical #DTS1070) for characterization.

Scaffold loading

Loading buffers were formulated in Milli-Q water: HEPES (500 mM) and HEPES-NaCl (500 mM HEPES, 400 mM NaCl) were formulated using, HEPES (Millipore Sigma #H4034) and Sodium Chloride (Fisher Scientific # BP358-1). For all imaging, elemental analysis, and cell-based experiments, the scaffolds had a size of 6 mm diameter × 0.35 mm thickness, and were cut from the electrospun mat using a biopsy punch (Integra #33-36). For scaffold loading by incubation, the scaffold disks were placed in a round-bottom 96-well plate. 200 μL of nanoparticle solution at the desired concentration was added and scaffolds were incubated for 1 hour, after which they were washed three times with MilliQ water. For vacuum-assisted loading, 6 mm scaffold disks were transferred into separate 5 ml polypropylene round-bottom tubes (Corning # 352063). A nanoparticle solution at the desired concentration in loading buffer was added to the tube and capped. A 16-gauge needle was attached to a 50 mL syringe and inserted through the cap of the tube. Vacuum was achieved by pulling back on the plunger to the 20 mL mark. Agitation of the tube was performed by dragging it across the uneven surface of a 1.5 mL 60-well microtube rack (Millipore Sigma # HS29025D) three times to agitate it. This process was performed twice. The tubes were then incubated for one hour at 4 °C, after which the mixture was aspirated, and the scaffolds were rinsed three times with deionized water. Loaded scaffolds were stored in deionized water at 4 °C.

Characterization of particles de-adsorbed from scaffolds

Particles were coated on scaffolds as previously described and incubated in 2 mL Eppendorf tubes in 1 mL of 1× PBS at 4 °C

on a spinning rotary shaker. After 48 h, the PBS was collected and characterized with dynamic light scattering as previously described.

Separately, scaffolds were coated with liposomes and incubated on a rotary shaker at 4 °C in 1 mL of either 1× PBS or 70% ethanol. Solution was collected and replaced at each timepoint. Fluorescence of solution was measured at endpoint using a Qubit 4 Fluorometer (Invivogen), exciting with the red 635 nm laser for Cy5 liposomes.

Scaffold imaging

The CML and LbL CML nanoparticle-loaded scaffolds were air dried overnight prior to SEM sample preparation. The samples were 8–10 nm sputter-coated with gold-palladium (Cressington sputter coater-108 auto) and imaged using Zeiss Sigma VP SEM with an accelerating voltage of 5 kV. At least $n = 2$ images were captured on two different areas from each scaffold with approximately 1500× and 7000× magnification.

Fluorescent liposome-coated scaffolds and fluorescent fluosphere (fluorescent CML)-coated scaffolds (Invivogen #F8801) were imaged using the Nikon Ti2 inverted microscope with AXR resonant spectral scanning confocal unit with laser emission range 662 nm–737 nm. Scaffolds were prepared on a microscope slide and imaged through a coverslip. At least $n = 2$ scaffolds were imaged per condition. 50 μm *z*-stacks were acquired to create maximum intensity projections. Images were denoised by the Nikon software and processed using FIJI-ImageJ. Fluorescence was then quantified with FIJI-ImageJ software: briefly, flattened images were converted to 16-bit images, background was subtracted with a rolling ball radius of 50.0 pixels, and fluorescence was measured. Reported values are intensity density per unit area, or mean intensity density.

Elemental analysis

Energy dispersive spectroscopy (EDS) was used for quantitative analysis of liposome-coating. Liposome-coated scaffolds were dried for 48 hours prior to analysis. Samples were coated with 10 nm carbon and imaged using the Screening Cube II (SRAMM). EDS measurements were collected with 20 000 counts at approximately 8100× magnification. $n = 2$ samples were prepared for each group, and an unpaired Student's *t*-test was performed.

Piezoelectric coefficient (d_{33}) measurements

Unpoled scaffolds were cut into 12 mm diameter × 0.35 mm thickness disks, and the piezoelectric coefficient was measured with a piezometer (Piezotest-PM300). The scaffolds were then coated with liposomes using our vacuum-assisted loading technique, airdried overnight, and remeasured.

Cell culture

HEK Blue™ CD122/CD132 (Invivogen #hkb-il2bg) cells were maintained in Dulbecco's modified Eagle's medium (DMEM) (Corning #10-014-CM) with 10% heat-inactivated fetal bovine serum (Fisher Scientific #A5256701), 100 U mL^{-1} penicillin, 100 μg mL^{-1} streptomycin (Thermo Fisher Scientific # 15140122) 2 mM L-glutamine (Millipore Sigma #G7513), 100 μg mL^{-1} Normocin™ (Invivogen #ant-nr), supplemented with 1× HEK-Blue™ Selection (Invivogen #hb-sel) and 1 μg mL^{-1} Puromycin (Invivogen #ant-pr) to select for reporter cells. Cells were tested for mycoplasma and maintained at 37 °C and 5% CO_2.

Cell viability

Cationic liposomes were formulated in sterile HEPES-NaCl (500 mM HEPES 400 mM NaCl) buffer. UV-treated scaffolds were loaded with liposomes or sterile buffer *via* vacuum-assisted loading for each time point. HEK Blue™ CD122/CD132 (Invivogen #hkb-il2bg) cells were plated on scaffolds, and this procedure was repeated every other day, in addition to replacing the cell media in each scaffold well, to enable a comparable readout at the end timepoint. Eight days after plating the first timepoint, Apexbio Technology LLC Cell Counting Kit-8 (CCK-8) reagent (Fisher Scientific #50-190-5565) was added to the scaffold-cell solution achieve a final concentration of 10% CCK-8 reagent in the cell culture well. A standard curve was generated to interpolate cell count values using simple linear regression. The plate was agitated and incubated for three hours at 37 °C, at which point the plate was agitated again in the Synergy Neo2 Plate reader, scaffolds were removed, and endpoint absorbance was read at 450 nm.

Cell signaling assay

Scaffolds were punched using 6 mm biopsy punches (Integra Life Sciences #33-36) and UV-treated for 15 min on each side. Liposomes were incubated with recombinant histidine-tagged human IL-15 (Sino Biological #10360-H07E) overnight at 4 °C to achieve a concentration of 180 ng mL^{-1} IL-15 on liposomes at 2 mg mL^{-1}, the loading concentration, in HEPES-NaCl. Scaffolds were coated with IL-15 liposomes as previously described with sterile vacuum-assisted loading techniques and were placed in flat-bottom propylene non-TC treated 96-well plates (Fisher Scientific cat#07-200-696). Scaffolds were incubated with complete media overnight at 4 °C. Media was removed, and 50 000 HEK-Blue CD122/CD132 (Invivogen #hkb-il2bg) cells at passage 8 were added to the liposome-coated scaffolds, uncoated scaffolds, or soluble condition (containing 0.477 μM of IL-15, the amount of 100% loading efficiency of IL-15 on scaffolds) in 100 μL complete media without Normocin or selective antibiotics. Every 24 hours, the media was collected to be stored at 4 °C. One week after plating, QUANTI-Blue™ solution (Invivogen #rep-qbs) was prepared and incubated at a 10 : 1 ratio with collected media for 30 minutes at 37 °C. SEAP levels were obtained with endpoint absorbance readings using the Synergy Neo2 plate reader at 620 nm.

Author contributions

Sarah Payne Bortel (SB), Sumayia Saif Jaima Chowdhury (SSC), Jeremy Cheng (JC), Daniella Uvaldo (DU), Mackenzie Wright (MW), Anna Marie Kylat (AK), Treena Livingston Arinzeh (TA), Santiago Correa (SC). SB: conceptualization, data curation, formal

analysis, investigation, methodology, supervision, visualization, validation, writing – original draft. SSC: conceptualization, data curation, investigation, methodology, validation. JC: data curation, investigation, validation, methodology. DU: investigation, validation, methodology. MW: investigation, validation, methodology. AK: data curation. TA: conceptualization, funding acquisition, project administration, resources, supervision. SC: conceptualization, funding acquisition, project administration, resources, supervision, writing – review & editing.

Conflicts of interest

Columbia University has filed a patent application for technology based on this work.

Data availability

Data for this article, including imaging data, elemental analyses, cell signaling/viability, and materials characterization are available at the Open Science Framework at https://osf.io/83ujb/overview?view_only=30afac09f9ea46fcb4bedad6887b5d4a.

Supplementary information (SI), including further materials characteristics, images, and analyses, is available. See DOI: https://doi.org/10.1039/d5bm01563d.

Acknowledgements

This work was funded by Columbia University's Provost's Cluster Hire Pilot Award in the Area of STEM Research Support, as well as by NIH/NIBIB Trailblazer Award (R21EB034818). SSC, AK and TA are funded by the National Science Foundation Science and Technology Center – Center for Engineering Mechanobiology (CEMB), CMMI – 1548571. These studies used the Confocal and Specialized Microscopy Shared Resource of the Herbert Irving Comprehensive Cancer Center at Columbia University, funded in part through the NIH/NCI Cancer Center Support Grant P30CA013696. Some of this work was performed at the Simons Electron Microscopy Center at the New York Structural Biology Center, with major support from the Simons Foundation (SF349247). The authors acknowledge the use of facilities, including Zeiss Sigma VP SEM, supported by NSF through Columbia University, the Columbia Nano Initiative, and the Materials Research Science and Engineering Center DMR-2011738. The authors would like to acknowledge Yasaman Aghli for contribution on fabricating electrospun scaffold mats.

References

1 L. Cai, J. Xu, Z. Yang, R. Tong, Z. Dong, C. Wang and K. W. Leong, *MedComm (2020)*, 2020, **1**, 35–46.
2 J. M. H. Liu, X. Zhang, S. Joe, X. Luo and L. D. Shea, *J. Immunol. Regener. Med.*, 2018, **1**, 1–12.
3 Q. Shang, Y. Dong, Y. Su, F. Leslie, M. Sun and F. Wang, *Adv. Drug Delivery Rev.*, 2022, **185**, 114308.
4 H. Wang, A. J. Najibi, M. C. Sobral, B. R. Seo, J. Y. Lee, D. Wu, A. W. Li, C. S. Verbeke and D. J. Mooney, *Nat. Commun.*, 2020, **11**, 5696.
5 J. X. Zhong, P. Raghavan and T. A. Desai, *Regener. Eng. Transl. Med.*, 2023, **9**, 224–239.
6 K. Mujahid, I. Rana, I. H. Suliman, Z. Li, J. Wu, H. He and J. Nam, *ACS Appl. Bio Mater.*, 2024, **7**, 4944–4961.
7 J. M. Messina, M. Luo, M. S. Hossan, H. A. Gadelrab, X. Yang, A. John, J. R. Wilmore and J. Luo, *Cytokine Growth Factor Rev.*, 2024, **77**, 1–14.
8 T. Kuribayashi, *Lab. Anim. Res.*, 2018, **34**, 80–83.
9 J. Dholakia, A. C. Cohen, C. A. Leath, E. T. Evans, R. D. Alvarez and P. H. Thaker, *Curr. Oncol. Rep.*, 2022, **24**, 389–397.
10 A. Mishra, L. Sullivan and M. A. Caligiuri, *Clin. Cancer Res.*, 2014, **20**, 2044–2050.
11 P. V. Torres-Ortega, R. Del Campo-Montoya, D. Plano, J. Paredes, J. Aldazabal, M.-R. Luquin, E. Santamaría, C. Sanmartín, M. J. Blanco-Prieto and E. Garbayo, *Biomacromolecules*, 2022, **23**, 4629–4644.
12 C. J. Massena, S. K. Lathrop, C. J. Davison, R. Schoener, H. G. Bazin, J. T. Evans and D. J. Burkhart, *Chem. Commun.*, 2021, **57**, 4698–4701.
13 N. Monteiro, A. Martins, R. L. Reis and N. M. Neves, *Regener. Ther.*, 2015, **1**, 109–118.
14 M. J. Grace, S. Lee, S. Bradshaw, J. Chapman, J. Spond, S. Cox, M. Delorenzo, D. Brassard, D. Wylie, S. Cannon-Carlson, C. Cullen, S. Indelicato, M. Voloch and R. Bordens, *J. Biol. Chem.*, 2005, **280**, 6327–6336.
15 Y. Tsutsumi, M. Onda, S. Nagata, B. Lee, R. J. Kreitman and I. Pastan, *Proc. Natl. Acad. Sci. U. S. A.*, 2000, **97**, 8548–8553.
16 X. He, S. Xiong, Y. Sun, M. Zhong, N. Xiao, Z. Zhou, T. Wang, Y. Tang and J. Xie, *Pharmaceutics*, 2023, **15**, 1610.
17 A. Jash, A. Ubeyitogullari and S. S. H. Rizvi, *J. Mater. Chem. B*, 2021, **9**, 4773–4792.
18 A. E. Barberio, S. G. Smith, I. S. Pires, S. Iyer, F. Reinhardt, M. B. Melo, H. Suh, R. A. Weinberg, D. J. Irvine and P. T. Hammond, *Bioeng. Transl. Med.*, 2023, **8**, e10453.
19 H. Xing, K. Hwang and Y. Lu, *Theranostics*, 2016, **6**, 1336–1352.
20 M. Frick, C. Schwieger and C. Schmidt, *Angew. Chem., Int. Ed.*, 2021, **60**, 11523–11530.
21 N. Monteiro, A. Martins, R. L. Reis and N. M. Neves, *J. R. Soc. Interface*, 2014, **11**, 20140459.
22 C. Zylberberg and S. Matosevic, *Ther. Delivery*, 2017, **8**, 425–445.
23 L. Yang, X. Lin, J. Zhou, S. Hou, Y. Fang, X. Bi, L. Yang, L. Li and Y. Fan, *Biomaterials*, 2021, **271**, 120768.
24 M. Kang, C.-S. Lee and M. Lee, *Bioengineering*, 2021, **8**, 137.
25 R. Cheng, L. Liu, Y. Xiang, Y. Lu, L. Deng, H. Zhang, H. A. Santos and W. Cui, *Biomaterials*, 2020, **232**, 119706.
26 L. Suamte and P. J. Babu, *Nano TransMed*, 2024, 100055.
27 M. C. Phipps, W. C. Clem, J. M. Grunda, G. A. Clines and S. L. Bellis, *Biomaterials*, 2012, **33**, 524–534.

28 F. Zamani, M. Amani Tehran and A. Abbasi, *Prog. Biomater.*, 2021, **10**, 151–160.
29 D. Liang, B. S. Hsiao and B. Chu, *Adv. Drug Delivery Rev.*, 2007, **59**, 1392–1412.
30 S. M. Damaraju, Y. Shen, E. Elele, B. Khusid, A. Eshghinejad, J. Li, M. Jaffe and T. L. Arinzeh, *Biomaterials*, 2017, **149**, 51–62.
31 L. T. Beringer, X. Xu, W. Shih, W.-H. Shih, R. Habas and C. L. Schauer, *Sens. Actuators, A*, 2015, **222**, 293–300.
32 D. Mandal, S. Yoon and K. J. Kim, *Macromol. Rapid Commun.*, 2011, **32**, 831–837.
33 L. Persano, C. Dagdeviren, Y. Su, Y. Zhang, S. Girardo, D. Pisignano, Y. Huang and J. A. Rogers, *Nat. Commun.*, 2013, **4**, 1633.
34 S. Correa, K. Y. Choi, E. C. Dreaden, K. Renggli, A. Shi, L. Gu, K. E. Shopsowitz, M. A. Quadir, E. Ben-Akiva and P. T. Hammond, *Adv. Funct. Mater.*, 2016, **26**, 991–1003.
35 S. Correa, N. Boehnke, E. Deiss-Yehiely and P. T. Hammond, *ACS Nano*, 2019, **13**, 5623–5634.
36 R. Augustine, P. Dan, A. Sosnik, N. Kalarikkal, N. Tran, B. Vincent, S. Thomas, P. Menu and D. Rouxel, *Nano Res.*, 2017, **10**, 3358–3376.
37 G. G. Genchi, E. Sinibaldi, L. Ceseracciu, M. Labardi, A. Marino, S. Marras, G. De Simoni, V. Mattoli and G. Ciofani, *Nanomedicine*, 2018, **14**, 2421–2432.
38 Y. Bar-Cohen and Q. Zhang, *MRS Bull.*, 2008, **33**, 173–181.
39 C. Li, P.-M. Wu, S. Lee, A. Gorton, M. J. Schulz and C. H. Ahn, *J. Microelectromech. Syst.*, 2008, **17**, 334–341.
40 S. Correa, E. L. Meany, E. C. Gale, J. H. Klich, O. M. Saouaf, A. T. Mayer, Z. Xiao, C. S. Liong, R. A. Brown, C. L. Maikawa, A. K. Grosskopf, J. L. Mann, J. Idoyaga and E. A. Appel, *Adv. Sci.*, 2022, **9**, 2103677.
41 G. Decher, *Science*, 1997, **277**, 1232–1237.
42 J. Lipton, G.-M. Weng, J. A. Röhr, H. Wang and A. D. Taylor, *Matter*, 2020, **2**, 1148–1165.
43 J. Borges and J. F. Mano, *Chem. Rev.*, 2014, **114**, 8883–8942.
44 V. L. S. dos Santos, R. C. Araújo, E. S. Lisboa, A. M. Lopes, R. L. de Albuquerque-Júnior, J. C. Cardoso, C. Blanco-Llamero, T. A. Deshpande, H. O. W. Anderson, R. Priefer, E. B. Souto and P. Severino, *J. Drug Delivery Sci. Technol.*, 2024, **91**, 105243.
45 A. J. Lovinger, *Science*, 1983, **220**, 1115–1121.
46 S. W. Lee, B.-S. Kim, S. Chen, Y. Shao-Horn and P. T. Hammond, *J. Am. Chem. Soc.*, 2009, **131**, 671–679.
47 R. Calcutt, R. Vincent, D. Dean, T. L. Arinzeh and R. Dixit, *Sci. Adv.*, 2021, **7**, eabj1469.
48 R. Zhu and Z. Wang, in *Emerging 2D Materials and Devices for the Internet of Things*, ed. L. Tao and D. Akinwande, Elsevier, 2020, pp. 221–241.
49 J. C. Phillips and J. A. Van Vechten, *Phys. Rev. Lett.*, 1969, **23**, 1115–1117.
50 N. Bhadwal, R. Ben Mrad and K. Behdinan, *Nanomaterials*, 2023, **13**, 3170.
51 G. B. Sukhorukov, E. Donath, S. Davis, H. Lichtenfeld, F. Caruso, V. I. Popov and H. Möhwald, *Polym. Adv. Technol.*, 1998, **9**, 759–767.
52 F. Caruso, R. A. Caruso and H. Mohwald, *Science*, 1998, **282**, 1111–1114.
53 E. Stellwagen, J. D. Prantner and N. C. Stellwagen, *Anal. Biochem.*, 2008, **373**, 407–409.
54 R. Zhu, Z. Wang, H. Ma, G. Yuan, F. Wang, Z. Cheng and H. Kimura, *Nano Energy*, 2018, **50**, 97–105.
55 X. Yang, J. D. Shah and H. Wang, *Tissue Eng., Part A*, 2009, **15**, 945–956.
56 Y. B. Truong, V. Glattauer, K. L. Briggs, S. Zappe and J. A. M. Ramshaw, *Biomaterials*, 2012, **33**, 9198–9204.
57 S. Catros, F. Guillemot, A. Nandakumar, S. Ziane, L. Moroni, P. Habibovic, C. van Blitterswijk, B. Rousseau, O. Chassande, J. Amédée and J.-C. Fricain, *Tissue Eng., Part C*, 2012, **18**, 62–70.
58 G. G. Flores-Rojas, B. Gómez-Lazaro, F. López-Saucedo, R. Vera-Graziano, E. Bucio and E. Mendizábal, *Macromolecules*, 2023, **3**, 524–553.
59 W. Ji, Y. Sun, F. Yang, J. J. J. P. van den Beucken, M. Fan, Z. Chen and J. A. Jansen, *Pharm. Res.*, 2011, **28**, 1259–1272.
60 H. Nie and C.-H. Wang, *J. Controlled Release*, 2007, **120**, 111–121.
61 H. Nie, M.-L. Ho, C.-K. Wang, C.-H. Wang and Y.-C. Fu, *Biomaterials*, 2009, **30**, 892–901.
62 S. Sakai, Y. Yamada, T. Yamaguchi, T. Ciach and K. Kawakami, *J. Biomed. Mater. Res., Part A*, 2009, **88A**, 281–287.
63 J. Zeng, A. Aigner, F. Czubayko, T. Kissel, J. H. Wendorff and A. Greiner, *Biomacromolecules*, 2005, **6**, 1484–1488.
64 Y. Yang, X. Li, W. Cui, S. Zhou, R. Tan and C. Wang, *J. Biomed. Mater. Res., Part A*, 2008, **86A**, 374–385.
65 Y. Li, H. Jiang and K. Zhu, *J. Mater. Sci.:Mater. Med.*, 2008, **19**, 827–832.
66 L. Xiaoqiang, S. Yan, C. Rui, H. Chuanglong, W. Hongsheng and M. Xiumei, *J. Appl. Polym. Sci.*, 2009, **111**, 1564–1570.
67 H. Li, C. Zhao, Z. Wang, H. Zhang, X. Yuan and D. Kong, *J. Biomater. Sci., Polym. Ed.*, 2010, **21**, 803–819.
68 I. Liao, S.Y Chew and K. Leong, *Nanomedicine*, 2006, **1**, 465–471.
69 J. Suk Choi and H. Sang Yoo, *J. Bioact. Compat. Polym.*, 2007, **22**, 508–524.
70 D. Grafahrend, J. L. Calvet, K. Klinkhammer, J. Salber, P. D. Dalton, M. Möller and D. Klee, *Biotechnol. Bioeng.*, 2008, **101**, 609–621.
71 W. Li, Y. Guo, H. Wang, D. Shi, C. Liang, Z. Ye, F. Qing and J. Gong, *J. Mater. Sci.:Mater. Med.*, 2008, **19**, 847–854.
72 X. Hu, T. Wang, F. Li and X. Mao, *RSC Adv.*, 2023, **13**, 20495–20511.
73 M. Alavi, N. Karimi and M. Safaei, *Adv. Pharm. Bull.*, 2017, **7**, 3–9.
74 G. Bozzuto and A. Molinari, *Int. J. Nanomed.*, 2015, **10**, 975–999.
75 S. Correa, A. K. Grosskopf, J. H. Klich, H. Lopez Hernandez and E. A. Appel, *Matter*, 2022, **5**, 1816–1838.
76 H. Nsairat, D. Khater, U. Sayed, F. Odeh, A. Al Bawab and W. Alshaer, *Heliyon*, 2022, **8**, e09394.

77 J. Tien, A. Terfort and G. M. Whitesides, *Langmuir*, 1997, **13**, 5349–5355.
78 Z. J. Jakubek, S. Chen, J. Zaifman, Y. Y. C. Tam and S. Zou, *Langmuir*, 2023, **39**, 2509–2519.
79 S. Wu, M.-S. Chen, P. Maurel, Y. Lee, M. Bartlett Bunge and T. L. Arinzeh, *J. Neural. Eng.*, 2018, **15**, 056010.
80 Y.-S. Lee, G. Collins and T. L. Arinzeh, *Acta Biomater.*, 2011, **7**, 3877–3886.
81 O. Gryshkov, F. Al Halabi, A. I. Kuhn, S. Leal-Marin, L. J. Freund, M. Förthmann, N. Meier, S.-A. Barker, K. Haastert-Talini and B. Glasmacher, *Int. J. Mol. Sci.*, 2021, **22**(21), 11373.
82 Q. Ni, K. Wagh, A. Pathni, H. Ni, V. Vashisht, A. Upadhyaya and G. A. Papoian, *eLife*, 2022, **11**, e82658.
83 S. Maric, T. K. Lind, M. R. Raida, E. Bengtsson, G. N. Fredrikson, S. Rogers, M. Moulin, M. Haertlein, V. T. Forsyth, M. R. Wenk, T. G. Pomorski, T. Arnebrant, R. Lund and M. Cárdenas, *Sci. Rep.*, 2019, **9**, 7591.
84 R. Tenchov, R. Bird, A. E. Curtze and Q. Zhou, *ACS Nano*, 2021, **15**, 16982–17015.
85 A. Gonçalves, R. Machado, A. C. Gomes and A. da Costa, *Appl. Sci.*, 2020, **10**, 7098.
86 P.-Y. Perera, J. H. Lichy, T. A. Waldmann and L. P. Perera, *Microbes Infect.*, 2012, **14**, 247–261.
87 H. Kanegane and G. Tosato, *Blood*, 1996, **88**, 230–235.
88 W. E. Carson, J. G. Giri, M. J. Lindemann, M. L. Linett, M. Ahdieh, R. Paxton, D. Anderson, J. Eisenmann, K. Grabstein and M. A. Caligiuri, *J. Exp. Med.*, 1994, **180**(4), 1395–1403.